Continuous radio frequency electric-field detection through adjacent Rydberg resonance tuning

Matthew T. Simons,* Alexandra B. Artusio-Glimpse, and Christopher L. Holloway
National Institute of Standards and Technology, Boulder, CO 80305, USA

Eric Imhof and Steven R. Jefferts
Northrop Grumman, Woodland Hills, CA, USA

Robert Wyllie and Brian C. Sawyer
Georgia Tech Research Institute, Atlanta, Georgia 30332, USA

Thad G Walker
Dept. of Physics, University of Wisconsin-Madison, Madison, WI 53706
(Dated: October 9, 2021)

We demonstrate the use of multiple atomic-level Rydberg-atom schemes for continuous frequency detection of radio frequency (RF) fields. Resonant detection of RF fields by electromagnetically-induced transparency and Autler-Townes (AT) in Rydberg atoms is typically limited to frequencies within the narrow bandwidth of a Rydberg transition. By applying a second field resonant with an adjacent Rydberg transition, far-detuned fields can be detected through a two-photon resonance AT splitting. This two-photon AT splitting method is several orders of magnitude more sensitive than off-resonant detection using the Stark shift. We present the results of various experimental configurations and a theoretical analysis to illustrate the effectiveness of this multiple level scheme. These results show that this approach allows for the detection of frequencies in continuous band between resonances with adjacent Rydberg states.

I. INTRODUCTION

Rydberg atoms have been increasingly investigated as radio frequency (RF) field sensors [1–10]. Rydberg atoms can detect microwave fields through both a Stark shift due to their polarizability [11–13] and Autler-Townes (AT) splitting [14–16] from resonant transitions. Resonant interactions are much more sensitive than the Stark effect, though they are limited to detection of discrete frequencies. However, Rydberg states can have strong couplings to many nearby states [17]. We show that by coupling multiple Rydberg levels we can effectively extend the frequency range of the resonant interaction, increasing the sensitivity to microwave fields far-detuned from a resonance transition. This paper discusses the architecture of this multi-level Rydberg system and nuances of tuning sensitivity to off-resonant signals using AT splitting.

The typical Rydberg atom-based RF electric (E) field detection technique relies on a 4-level electromagnetically-induced transparency (EIT) scheme, as shown in Fig. 1(a). This scheme includes a ground-state probe laser (which couples levels $|1\rangle$ and $|2\rangle$), a coupling laser that couples to a Rydberg state ($|3\rangle$, coupled from level $|2\rangle$), and the RF field of interest (signal field, or SIG) which couples two Rydberg states (levels $|3\rangle$ and $|4\rangle$). The addition of the resonant RF field (labeled as ω_{SIG}) results in AT splitting. The AT
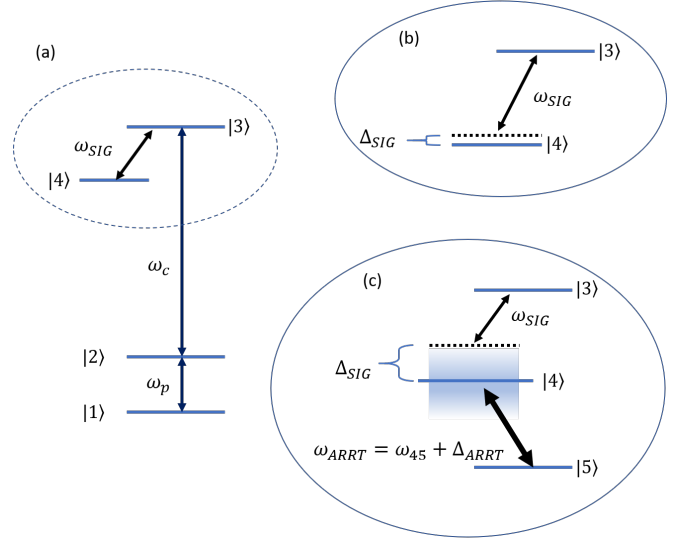

FIG. 1. (a) Typical 4-level EIT/AT scheme where ω_p and ω_c are the optical probe and pump fields and ω_{SIG} is the RF signal that causes AT splitting for detection. (b) The RF field can be detuned over a small range from the $|3\rangle - |4\rangle$ transition and still cause AT splitting. (c) This range can be extended by coupling to an adjacent resonance, $|4\rangle - |5\rangle$.

split gives a direct SI-traceable measurement of the SIG RF E-field strength [2, 3, 16, 18].

Using standard EIT/AT techniques, E-field strength can be routinely measured down to a few mV/cm [2, 16, 18, 19]. With optical homodyne [20] or RF heterodyne (a Rydberg atom-based mixer) [21, 22] techniques with EIT,
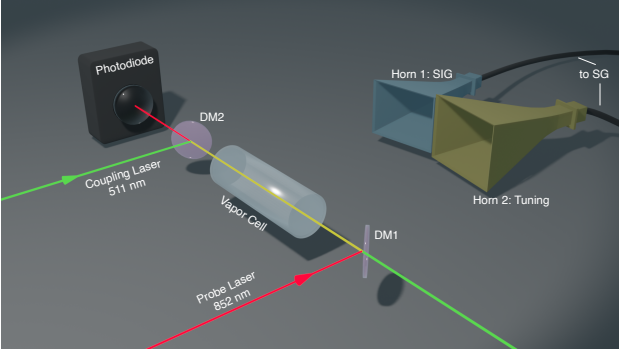
---

* matthew.simons@nist.gov

FIG. 3. Experimental setup of the five-level EIT scheme. SG: signal generator, DM: dichroic mirror.

$6\ S_{1/2}(F\ =\ 4)\ \rightarrow\ 6\ P_{3/2}(F\ =\ 5)$ with a wavelength of $\lambda_p\ =\ 852.35$ nm [25]. To produce an EIT signal, we apply a counter-propagating coupling laser with $\lambda_c \approx 508.98$ nm and scan it across the $6\ P_{3/2} \rightarrow 68\ S1/2$ Rydberg transition. We use a lock-in amplifier to enhance the EIT signal-to-noise ratio by modulating the coupling laser amplitude with a 37 kHz square wave with a 50 % duty cycle. This removes the background and isolates the EIT signal. RF sources are used to couple to the Rydberg states $|3\rangle$, $|4\rangle$ and $|5\rangle$. To generate these RF fields, the output of two signal generators (SG) are connected to two different horn antennas (referred to as Horn 1 and Horn 2). Horn 1 and Horn 2 were placed 23 cm and 21 cm from the laser beam locations in the vapor cell, respectively. Horn 1 produces the SIG field coupling Rydberg states $|3\rangle$ and $|4\rangle$. Horn 2 produces the ARRT field used to couple Rydberg states $|4\rangle$ and $|5\rangle$. In these experiments, the optical beams and the RF electric fields are co-linearly polarized, in that the E-field vectors are all pointing in the same direction. In our case, the E-field vectors are pointing up from the optics table, perpendicular to the plane that contains all of the propagation vectors.

III. EXPERIMENTAL RESULTS

Continuous frequency detection for the SIG field (which couples states $|3\rangle$ and $|4\rangle$) can be achieved either by varying the Rabi frequency of the ARRT field or detuning the ARRT field from resonance with the $|4\rangle \rightarrow |5\rangle$ transition. In this section we investigate both approaches.

A. Detuning the Frequency of the ARRT field

When the ARRT field is off, the measurements of AT-splitting versus the SIG detuning (Δ_{SIG}) are shown in Fig. 2 (top), for a given Rabi frequency. The asymmetric amplitudes of the peaks illustrate that without the ARRT field, the AT peaks are difficult to resolve when ω_{SIG}
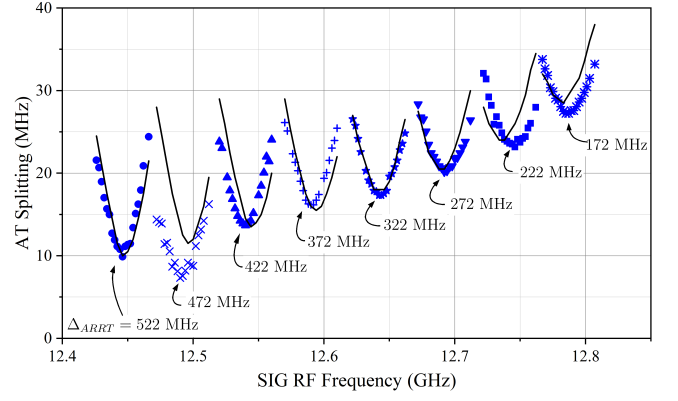
FIG. 4. SIG detuning Δ_{SIG} for various values of Δ_{ARRT}. Each parabola represents a different value of Δ_{ARRT}, while the AT splitting was measured as Δ_{SIG} was swept. Each one follows the same function as the zero-detuning case in Fig. 2 (top), where the AT splitting is a minimum on resonance. This shows that there is an apparent resonance condition that is shifted by applying the ARRT field. A description of the numerical model used to generate the simulated results (solid lines) is given in Section IV.
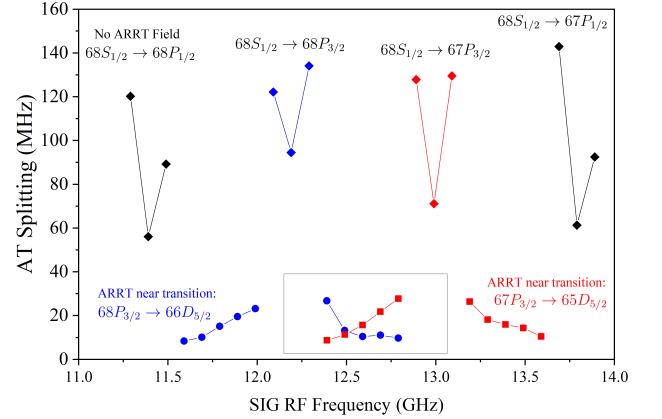
FIG. 5. Measurements of the AT splitting by a SIG field from both direct resonances (diamonds) and with an ARRT field (squares and circles). The blue circles are AT splittings enabled by applying an ARRT field near the $68\ P_{3/2} - 66\ D_{5/2}$ transition to shift the $68P_{3/2}$ state, and the red squares were made using an ARRT field near the $67\ P_{3/2} - 65\ D_{5/2}$ transition to shift the $67\ P_{3/2}$ state. This shows that the application of an appropriate adjacent resonance field can enable resonant detection over a continuous frequency range spanning several Rydberg states.

is within ± 50 MHz of the transition frequency for the $68\ S_{1/2} \leftrightarrow 67\ P_{3/2}$ states.

However, by applying an ARRT field to shift the Rydberg state, the frequency range for which a SIG field can be detected dramatically increases, as illustrated in Fig. 4. Here we plot several Δ_{SIG} curves [similar to the one given in Fig. 2(a)] for different values of the ARRT field detuning (Δ_{ARRT}). In these data, $|4\rangle \leftrightarrow |5\rangle$ corresponds to $67\ P_{3/2} - 65\ D_{5/2}$ with fre-

quency $\omega_{45} = 23.89$ GHz. In fact, by varying Δ_{ARRT}, it is possible to detect a signal over a continuous frequency that spans from one principal quantum number n (for $|3\rangle \leftrightarrow |4\rangle$) to another by simply changing Δ_{ARRT}. This is shown in Fig. 5 where we show continuous frequency detection from 11.25 to 13.9 GHz by measuring an AT splitting either directly or enabled by an ARRT field. Keeping Ω_{ARRT} constant and relatively low, the optimal detection of a particular Δ_{SIG} occurs for $\Delta_{ARRT} = \pm\Delta_{SIG}$, as shown in Fig. 6. In these results we see that if we use $|3\rangle = 68S_{1/2}$, $|4\rangle = 68P_{3/2}$, and $|5\rangle = 66\ D_{5/2}$, an increase in Δ_{ARRT} corresponds to a linear increase in the detectable frequency detuning for SIG. When we switch to $|4\rangle = 67\ P_{3/2}$ and $|5\rangle = 65\ D_{5/2}$, a decrease in Δ_{ARRT} corresponds to a linear decrease in the detectable frequency detuning for SIG. These results were obtained by measuring the minimum AT-splitting as the ARRT field detuning was varied for various SIG field detunings. This is analogous to finding the minimum AT-splitting in Fig. 2 (top), which corresponds to the resonant frequency. Here the 'resonant' frequency changes with the application of the ARRT field. Within a $|\Delta_{SIG}| < 200$ MHz, the splitting enabled by the ARRT field was not resolvable because the SIG field was strong enough to cause a large AT-splitting of the $|3\rangle \rightarrow |4\rangle$ transition. This approach can be used to measure continuous frequencies for the SIG field over several Rydberg states. This is shown in Fig. 5.
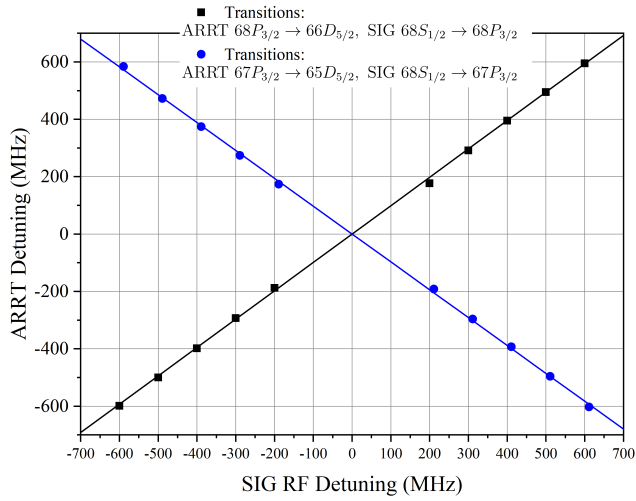
FIG. 6. ARRT detunings that give symmetric AT splitting versus SIG detuning. The lines are linear fits to the measured data. The 68 $P_{3/2}$ is higher in energy than the 68 $S_{1/2}$ state, so there is a linear relationship in the two-photon detuning, while the 67 $P_{3/2}$ is lower in than the 68 $S_{1/2}$ state, so the two-photon detuning has an inverse relationship. Uncertainty in these measurements is determined by the dependence of the AT splitting on the RF frequencies, which near resonance is on the order of ~ 5 MHz.

B. Power Tuning of the ARRT field

The two-photon response can also be achieved by varying the Rabi frequency of the ARRT field, Ω_{ARRT}. In this case we leave the frequency of the ARRT field resonant with the tuning transition ($\Delta_{ARRT} = 0$), and vary the power delivered to the ARRT field horn antenna in order to maximize the EIT response for a given Δ_{SIG}. To measure this effect, we work with weak SIG strengths such that they do not cause AT splitting, but do reduce the height of the EIT peak. Fig. 7 shows the reduction in EIT height (where a positive value reflects a decrease in the EIT height) versus Ω_{ARRT}, for nine different Δ_{SIG}. As the SIG field is detuned away from resonance, the ARRT field strength must be increased in order to see an optimal two-photon coupling between the three Rydberg levels. Fig. 8 shows that the optimal ARRT field strength varies linearly with Δ_{SIG}.
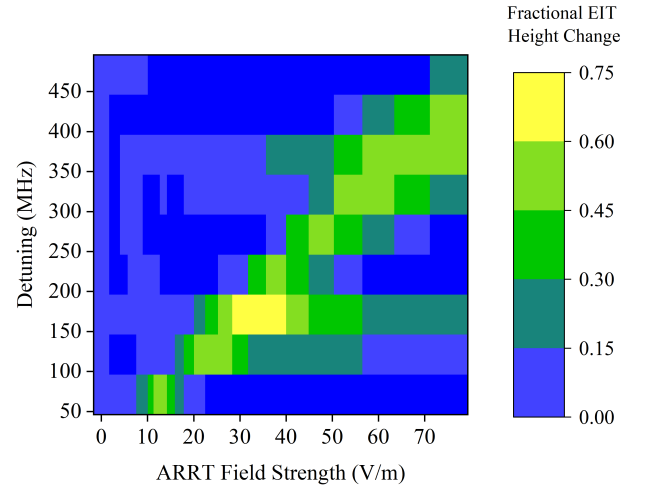
FIG. 7. Fractional reduction in EIT amplitude (change in EIT amplitude over the unperturbed amplitude) versus ARRT field Rabi frequency Ω_{ARRT} and SIG field detunings Δ_{SIG}. The maximum EIT amplitude reduction for a given Δ_{SIG} occurs at a larger Ω_{ARRT} as the detuning increases.

We can also vary both field strength and frequency of the ARRT field to maximize sensitivity to SIG field. Fig. 9 shows how the ARRT field Rabi frequency affects the optimal ARRT field detuning Δ_{ARRT}. For weak Ω_{ARRT} the optimal Δ_{ARRT} varies linearly with Δ_{SIG}, especially far from the on-resonance condition for the SIG field, as shown in the previous section. However, for a strong Ω_{ARRT} the optimal Δ_{ARRT} is shifted lower and becomes increasingly nonlinear near the $\Delta_{SIG} = 0$ resonance.

C. Uncertainties

A discussion of the contributions to the uncertainties of the Autler-Townes splitting measurement can be found
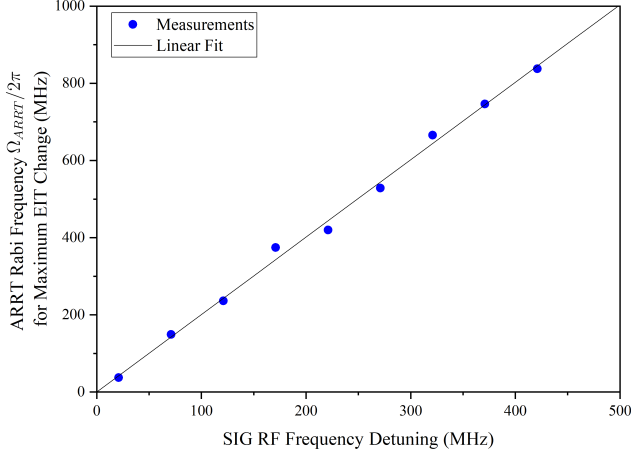
FIG. 8. The ARRT field Rabi frequency Ω_{ARRT} for maximum sensitivity increases linearly with SIG field detunings Δ_{SIG}.
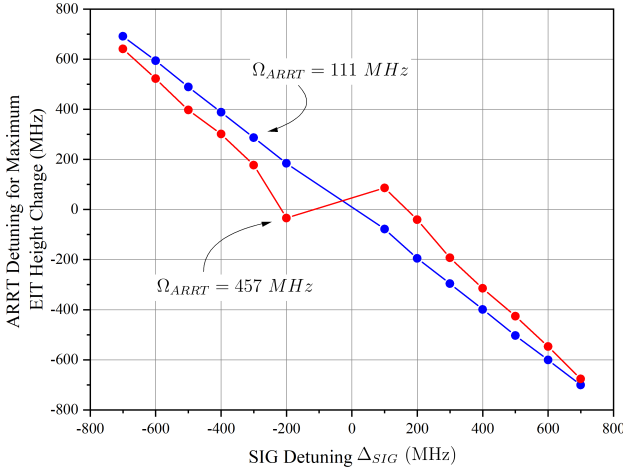
FIG. 9. ARRT field detuning Δ_{ARRT} is varied to maximize response to various SIG field detunings Δ_{SIG}, for two ARRT field strengths. For a weak ARRT field, optimal Δ_{ARRT} varies linearly with the detuning of the SIG field. For a strong ARRT field, optimal Δ_{ARRT} is reduced, and becomes non-linear. The asymmetry is likely due to an AC stark shift caused by the strong ARRT field.

in [16] and [26]. Measurements of the AT splitting in this paper have an uncertainty of ~ 1 %, arising from the uncertainty in peak fitting and in the frequency scale. There can be large uncertainty arising from the perturbation of the RF field due to the dielectric vapor cell, which affects the determination of the field strength from the AT measurement. In these experiments, there is uncertainty in the Rabi frequencies of the ARRT and the SIG due to the different standing wave patterns inside the vapor cell. This is one significant source of disagreement between the models and experiment. Further work will analyze uncertainty contributions for this ARRT method of field
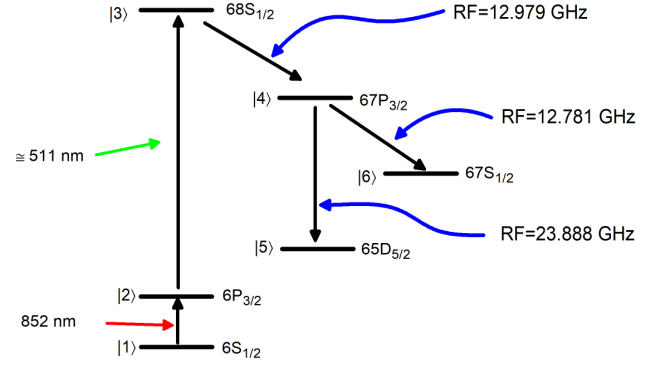
FIG. 10. Six-level scheme used to model the experimental data.

strength detection, in comparison to the contributions for the standard AT method.

IV. THEORETICAL MODELING

We present a theoretical model to depict the observed continuous frequency detection shown in the experimental results. Note that for the Rydberg states used in these experiments, the frequency of SIG field can simultaneously couple to two sets of states, $68\,S_{1/2} - 67\,P_{3/2}$ and $67\,S_{1/2} - 67\,P_{3/2}$. This is due to the fact that the difference between the transition frequencies of these two sets of states is 198 MHz (see Fig. 10) and these transitions have similar dipole moments (d). The radial part of d for the two states are $d = 4396.3\,e\,a_o$ for $68\,S_{1/2} - 67\,P_{3/2}$ and $d = 4500.9\,e\,a_o$ for $67\,S_{1/2} - 67\,P_{3/2}$, where e is the elementary charge (in units of C) and a_0 is the Bohr radius (in units of m). Given that the SIG field couples to both these states, Rabi frequencies for the two transitions are related by the ratio of these two dipole moments and given by

$$\Omega_{RF46} = 1.02\,\Omega_{RF34} = 1.02\,\Omega_{SIG} \qquad (1)$$

To account for this potential simultaneous coupling, we model the six-level scheme shown in Fig.10. The model used here is similar to the one presented [17, 27], where the main difference is the atomic species used. In the model for the experimental results of the paper, we use ^{133}Cs, while in Refs. [17, 27] ^{85}Rb is used. For this six-level ^{133}Cs model we follow a similar process to the one given in [17, 27] and we start by noting that the power of the probe beam measured on the detector (the EIT signal, i.e., the probe transmission through the vapor cell) is given by [28]

$$P = P_0 \exp\left(-\frac{2\pi L\,\text{Im}\,[\chi]}{\lambda_p}\right) = P_0 \exp\left(-\alpha L\right)\ , \qquad (2)$$

where P_0 is the power of the probe beam at the input of the cell, L is the length of the cell, λ_p is the wavelength

of the probe laser, χ is the susceptibility of the medium seen by the probe laser, and $\alpha = 2\pi \mathrm{Im}\left[\chi\right]/\lambda_p$ is Beer's absorption coefficient for the probe laser. The susceptibility for the probe laser is related to the density matrix component (ρ_{21}) by the following [28]

$$\chi = \frac{2\mathcal{N}_0 \wp_{12}}{E_p \epsilon_0} \rho_{21_D} = \frac{2\mathcal{N}_0}{\epsilon_0 \hbar}\frac{(d\,e\,a_0)^2}{\Omega_p}\rho_{21_D} \ , \qquad (3)$$

where $d = 2.02$[25] is the normalized transition-dipole moment for the probe laser, Ω_p is the Rabi frequency for the probe laser in units of rad/s. The subscript D on ρ_{21} presents a Doppler averaged value. $\mathcal{N}_0$ is the total density of atoms in the cell and is given by

$$\mathcal{N}_0 = \frac{p}{k_B T} \ , \qquad (4)$$

where k_B is the Boltzmann constant, T is temperature in Kelvin, and the pressure p (in units of Pa) is given by [25]

$$p = 10^{9.717 - \frac{3999}{T}} \qquad (5)$$

In eq. (3), $\wp_{12}$ is the transition-dipole moment for the $|1\rangle$-$|2\rangle$ transition, ϵ_0 is the vacuum permittivity, and E_p is the amplitude of the probe laser E-field.

The density matrix component (ρ_{21}) is obtained from the master equation [28]

$$\dot{\rho} = \frac{\partial \rho}{\partial t} = -\frac{i}{\hbar}\left[H, \rho\right] + \mathcal{L} \ , \qquad (6)$$

where H is the Hamiltonian of the atomic system under consideration and $\mathcal{L}$ is the Lindblad operator that accounts for the decay processes in the atom.

For the six-level system shown in Fig. 10, the Hamiltonian can be expressed as:

$$H = \frac{\hbar}{2}\begin{bmatrix} 0 & \Omega_p & 0 & 0 & 0 & 0 \\ \Omega_p & A & \Omega_c & 0 & 0 & 0 \\ 0 & \Omega_c & B & \Omega_{SIG34} & 0 & 0 \\ 0 & 0 & \Omega_{SIG34} & C & \Omega_{ARRT} & \Omega_{SIG46} \\ 0 & 0 & 0 & \Omega_{ARRT} & D & 0 \\ 0 & 0 & 0 & \Omega_{SIG46} & 0 & E \end{bmatrix} ,$$

$$(7)$$

where Ω_p, Ω_c, and Ω_{SIG} are the Rabi frequencies of the probe laser, coupling laser, and ARRT field coupled states, respectively. Also,

$$\begin{aligned} A &= 2\Delta_p \\ B &= -2(\Delta_p + \Delta_c) \\ C &= -2(\Delta_p + \Delta_c + \Delta_{SIG34}) \\ D &= -2(\Delta_p + \Delta_c + \Delta_{SIG34} + \Delta_{ARRT}) \\ E &= -2(\Delta_p + \Delta_c + \Delta_{SIG34} + \Delta_{SIG46}) \ , \end{aligned} \qquad (8)$$

where Δ_p, Δ_c, and Δ_{ARRT} are the detunings of the probe laser, couple laser, and the ARRT field, respectively, defined as

$$\Delta_{p,c,ARRT} = \omega_{p,c,ARRT} - \omega_{12,23,45} \ , \qquad (9)$$

where $\omega_{12,23,45}$ are the on-resonance angular frequencies of transitions $|2\rangle$-$|3\rangle$, and $|4\rangle$-$|5\rangle$ for the probe, coupling, and ARRT fields, respectively, and $\omega_{p,c,T}$ are the angular frequencies of the probe, coupling, and ARRT fields, respectively. The SIG field detuning is defined as

$$\Delta_{SIG34} = \Delta_{SIG} = \omega_{SIG} - \omega_{34} \qquad (10)$$

for the $|3\rangle - |4\rangle$ transition, and detuning of the additional $|4\rangle - |6\rangle$ transition is defined as

$$\begin{aligned} \Delta_{SIG46} &= \omega_{SIG} - \omega_{46} \\ &= 2\pi \cdot [12.979 \text{ GHz} - 23.888 \text{ GHz}] + \Delta_{SIG}. \end{aligned} \qquad (11)$$
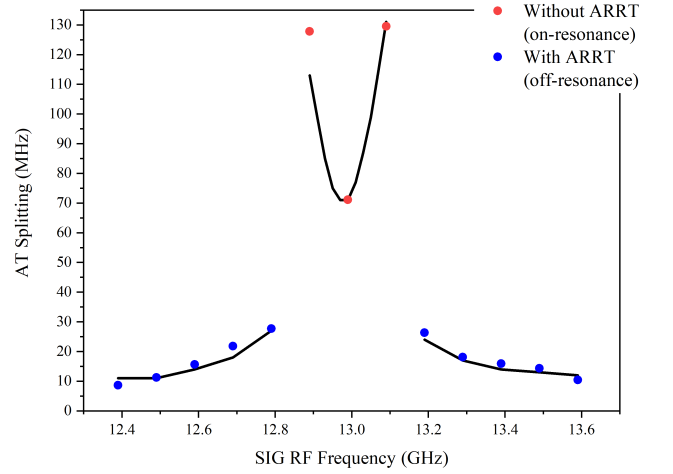
FIG. 11. Comparison of simulations (black lines) to experimental data (red and blue dots) in Fig. 5, from the SIG transition 68 $S_{1/2} - 67$ $P_{3/2}$ using an ARRT field near 67 $P_{3/2} - 65$ $D_{5/2}$. The AT splittings are predicted well by theory.

In our experiments, $\Delta_p = 0$ rad/s and Δ_c is scanned, while Δ_{SIG} and Δ_{ARRT} are varied. The optical Rabi frequencies are $\Omega_p/2\pi = 9.48$ MHz and $\Omega_c/2\pi = 0.564$ MHz for the probe and coupling lasers, respectively. The signal RF field Rabi frequency is generally held fixed at $\Omega_{SIG}/2\pi = 100$ MHz or thereabouts, while the ARRT field Rabi frequency Ω_T is varied.

For the six-level system, the $\mathcal{L}$ matrix is given in eq. (12), where $\gamma_{ij} = (\Gamma_i + \Gamma_j)/2$ and $\Gamma_{i,j}$ are the transition decay rates. Since the purpose of the present study is to explore the intrinsic limitations of Rydberg-EIT field sensing in vapor cells, no collision terms or dephasing terms are added. While Rydberg-atom collisions, Penning ionization, and ion electric fields can, in principle, cause dephasing, such effects can, for instance, be alleviated by reducing the beam intensities, lowering the vapor pressure, or limiting the atom-field interaction time. In this analysis we set, $\Gamma_1 = 0$, $\Gamma_2 = 2\pi \times (6 \text{ MHz})$, $\Gamma_3 = 2\pi \times (3 \text{ kHz})$, $\Gamma_{4,5,6} = 2\pi \times (2 \text{ kHz})$. Note, Γ_2 is for the D2 line in ^{133}Cs [25], and Γ_3, $\Gamma_{4,5,6}$, are typical Rydberg decay rates.

$$\mathcal{L} = \begin{bmatrix} \Gamma_2\rho_{22} & -\gamma_{12}\rho_{12} & -\gamma_{13}\rho_{13} & -\gamma_{14}\rho_{14} & -\gamma_{15}\rho_{15} & -\gamma_{16}\rho_{16} \\ -\gamma_{21}\rho_{21} & \Gamma_3\rho_{33} - \Gamma_2\rho_{22} & -\gamma_{23}\rho_{23} & -\gamma_{24}\rho_{24} & -\gamma_{25}\rho_{25} & -\gamma_{26}\rho_{26} \\ -\gamma_{31}\rho_{31} & -\gamma_{32}\rho_{32} & -\Gamma_3\rho_{33} & -\gamma_{34}\rho_{34} & -\gamma_{35}\rho_{35} & -\gamma_{36}\rho_{36} \\ -\gamma_{41}\rho_{41} & -\gamma_{42}\rho_{42} & -\gamma_{43}\rho_{43} & \Gamma_3\rho_{33} - \Gamma_4\rho_{44} & -\gamma_{45}\rho_{45} & -\gamma_{46}\rho_{46} \\ -\gamma_{51}\rho_{51} & -\gamma_{52}\rho_{52} & -\gamma_{53}\rho_{53} & -\gamma_{45}\rho_{45} & \Gamma_4\rho_{44} - \Gamma_5\rho_{55} & -\gamma_{56}\rho_{56} \\ -\gamma_{61}\rho_{61} & -\gamma_{62}\rho_{62} & -\gamma_{63}\rho_{63} & -\gamma_{65}\rho_{65} & -\gamma_{56}\rho_{56} & \Gamma_4\rho_{44} - \Gamma_6\rho_{66} \end{bmatrix} \quad (12)$$
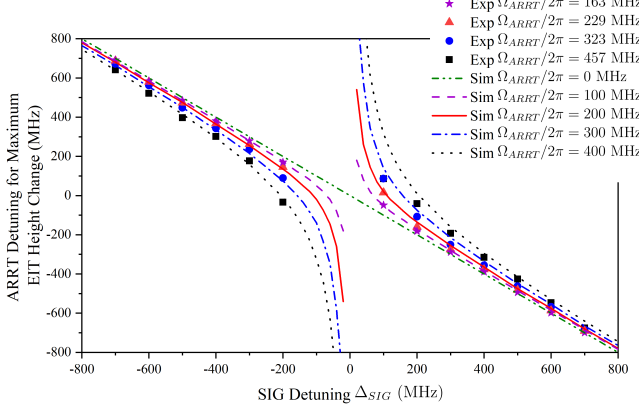

FIG. 12. Repeat of Fig. 9 with more Ω_T measurements and compared to the model calculations. The experimental measurements show an asymmetry with the sign of Δ_{SIG}, suggestive of a frequency shifting that the model does not capture, whereas the model does demonstrate the divergent trend as the SIG approaches the on-resonant condition (where the ARRT field is no longer beneficial).

We numerically solve these equations to find the steady-state solution for ρ_{21} for various values of Ω_{SIG}, Ω_{ARRT}, Δ_{SIG}, and Δ_{ARRT}. This is done by forming a matrix with the system of equations for $\dot{\rho}_{ij} = 0$. The null-space of the resulting system matrix is the steady-state solution. The steady-state solution for ρ_{21} is then Doppler averaged[28]

$$\rho_{21_D} = \frac{1}{\sqrt{\pi}\, u} \int_{-3u}^{3u} \rho_{21}\left(\Delta_p', \Delta_c'\right)\, e^{\frac{-v^2}{u^2}}\, dv \ , \qquad (13)$$

where $u = \sqrt{2k_B T/m}$ and m is the mass of the atom. We use the case where the probe and coupling laser are counter-propagating. Thus, the frequency seen by the atom moving toward the probe beam is upshifted by $2\pi v/\lambda_p$ (where v is the velocity of the atoms), while the frequency of the coupling beam seen by the same atom is downshifted by $2\pi v/\lambda_c$. The probe and coupling beam detuning is modified by the following

$$\Delta_p' = \Delta_p - \frac{2\pi}{\lambda_p} v \ \text{ and } \ \Delta_c' = \Delta_c + \frac{2\pi}{\lambda_c} v \ . \qquad (14)$$

Figure 11 shows a comparison of numerically generated results from the theoretical model and experimental data. A duplication of the 68 $S_{1/2} \rightarrow 67\ P_{3/2}$ state transition measurements from Fig. 5, this figure shows that the model reproduces the general effect of having the

ARRT field on for off-resonant detection of SIG. Similarly, Fig. 4 compares the model with measurements of AT splitting over a wide range of SIG detunings for a set of ARRT detunings with good agreement of the model to the experimental measurements. Small differences between the model and experimental results in this figure may be due to variations in the SIG or ARRT Rabi frequencies over the full range of SIG and ARRT frequencies. We also compare the measurements reported in Fig. 9 to the model in Fig. 12 and again see that the model recreates the measured trends. However, where an asymmetry was measured in the experiments (likely due to an AC stark shift caused by the tuning field) the model does not reproduce this effect.

A key benefit of having a theoretical model that reproduces experimental results of this kind is the ability to quickly study a wider parameter space than is feasible purely with experimental measurements. For example, we take the model results of Fig. 12 and calculate a contrast parameter for the change in EIT height given by

$$C = \frac{|T_{RF} - T_0|}{T_0}, \qquad (15)$$

where T_0 is the probe laser transmittance (P/P_0 from Eq. 2) for $\Delta_p = \Delta_c = 0$ rad/s with no RF fields ($\Omega_{SIG} = \Omega_T = 0$ rad/s) and T_{RF} is the same probe laser transmittance but with SIG and ARRT fields turned on. The sensitivity of a measurement of SIG is directly related to this contrast parameter such that high EIT contrast relates to a high sensitivity. Figure 13 gives the modeled calculations of contrast for the set of ARRT Rabi frequencies over a ± 800 MHz range of SIG detunings. We note that the model considers only the states defined in Fig. 10, so SIG detunings beyond this range are not well predicted by the model. It is clear from Fig. 13 that increasing the power (i.e., the Rabi frequency) of the ARRT field results in significant increases in contrast (or measurement sensitivity) for SIG fields that are highly detuned from resonance.

We can quantify the improvement obtained in the measurement by the incorporation of this ARRT field by calculating the contrast gain factor,

$$G = \frac{C_{tuner}}{C_0}, \qquad (16)$$

or the ratio of calculated contrast values with and without an ARRT field (no ARRT field is modeled by the orange curve in Fig. 12 and Fig. 13 where $\Omega_T/2\pi = 0$ MHz). These contrast gains calculated by our model are given in Fig. 14 for the same set of Ω_{ARRT} and SIG detunings.
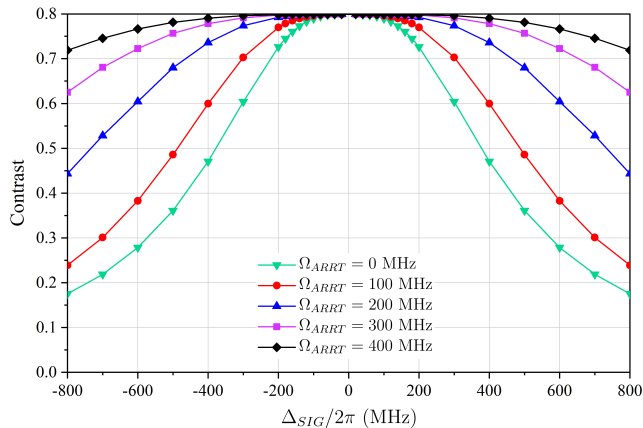
FIG. 13. Maximum EIT height change (from Fig. 12) reported as contrast (Eq. 15) for a set of SIG and ARRT Rabi frequencies (Ω_{SIG} and Ω_{ARRT}, respectively) over a wide range of SIG detunings (Δ_{SIG}). Increased contrast relates to an increase in sensitivity to the detuned SIG field.
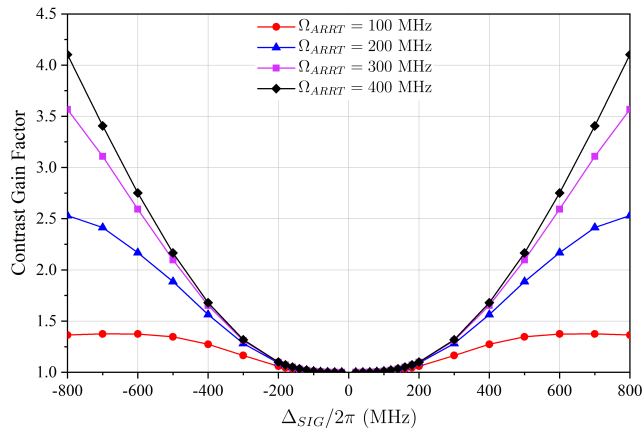

FIG. 14. Numerically modeled contrast gain factor (Eq. 16) for a set of ARRT field Rabi frequencies (Ω_T) over a wide range of SIG field detunings (Δ_{SIG}) showing increased sensitivity gain for strong ARRT fields and highly detuned SIG fields.

With a strong ARRT field, the EIT height change, or the contrast, is increased by as much as four times for highly detuned SIG fields. However, this also shows that there is not much gain for $\Delta_{SIG} < \pm 100$ MHz. At those detunings, the SIG field is close enough to resonance that the strong ARRT field does not improve the contrast.

V. CONCLUSION

In this paper, we demonstrate a five-level atomic scheme that allows for the resonant detection of an RF signal by Rydberg EIT over a continuous frequency range. The main Rydberg transition frequency is tuned by the presence of an adjacent Rydberg resonance tuning field. In this five-level scheme, we show continuous frequency detection can be obtained by either varying the frequency or the power level of the ARRT field. Notably, this technique allows for the detection of a signal RF field over a frequency range that covers from one Rydberg state with principal quantum number n to the next $n + 1$ state. The data in this paper show that the Autler-Townes tuning of Rydberg resonances allows for complete spectral coverage; the dressed states may be shifted by an amount corresponding to a change of the principal quantum number by 1 without significant degradation of the electric field sensitivity.

[1] A. Osterwalder and F. Merkt, Phys. Rev. Lett. **82**, 1831 (1999).

[2] C. Holloway, J. Gordon, S. Jefferts, A. Schwarzkopf, D. Anderson, S. Miller, N. Thaicharoen, and G. Raithel, Antennas and Propagation, IEEE Transactions on **62**, 6169 (2014).

[3] H. Fan, S. Kumar, J. Sedlacek, H. Kübler, S. Karimkashi, and J. Shaffer, J. Phys. B: At. Mol. Opt. Phys. **48**, 202001 (2015).

[4] D. A. Anderson, S. A. Miller, G. Raithel, J. A. Gordon, M. L. Butler, and C. L. Holloway, Phys. Rev. Applied **5**, 034003 (2016).

[5] K. C. Cox, D. H. Meyer, F. K. Fatemi, and P. D. Kunz, Phys. Rev. Lett. **121**, 110502 (2018).

[6] D. Meyer, K. Cox, F. Fatemi, and P. Kunz, Applied Physics Letters **12**, 211108 (2018).

[7] Z. Song, H. Liu, X. Liu, W. Zhang, H. Zou, J. Zhang, and J. Qu, Opt. Express **27**, 8848 (2019).

[8] D. H. Meyer, Z. A. Castillo, K. C. Cox, and P. D. Kunz, Journal of Physics B: Atomic, Molecular and Optical Physics **53**, 034001 (2020).

[9] M. T. Simons, A. H. Haddab, J. A. Gordon, and C. L. Holloway, Applied Physics Letters **114**, 114101 (2019), https://doi.org/10.1063/1.5088821.

[10] C. L. Holloway, M. T. Simons, J. A. Gordon, and D. Novotny, IEEE Antennas and Wireless Propagation Letters **18**, 1853 (2019).

[11] T. F. Gallagher, *Rydberg Atoms*, Cambridge Monographs on Atomic, Molecular and Chemical Physics (Cambridge University Press, Cambridge, 1994).

[12] D. H. Meyer, P. D. Kunz, and K. C. Cox, Phys. Rev. Applied **15**, 014053 (2021).

[13] D. A. Anderson and G. Raithel, Applied Physics Letters **111**, 053504 (2017), https://doi.org/10.1063/1.4996234.

[14] S. H. Autler and C. H. Townes, Phys. Rev. **100**, 703 (1955).

[15] M. Tanasittikosol, J. D. Pritchard, D. Maxwell, A. Gauguet, K. J. Weatherill, R. M. Potvliege, and C. S. Adams, Journal of Physics B: Atomic, Molecular and Optical Physics **44**, 184020 (2011).

[16] J. Sedlacek, A. Schwettmann, H. Kubler, R. Low, T. Pfau, and J. Shaffer, Nature Physics **8**, 819 (2012).

[17] A. K. Robinson, A. B. Artusio-Glimpse, M. T. Simons, and C. L. Holloway, Phys. Rev. A **103**, 023704 (2021).

[18] C. L. Holloway, M. T. Simons, J. A. Gordon, P. F. Wilson, C. M. Cooke, D. A. Anderson, and G. Raithel, IEEE Transactions on Electromagnetic Compatibility **59**, 717 (2017).

[19] C. L. Holloway, J. A. Gordon, A. Schwarzkopf, D. A. Anderson, S. A. Miller, N. Thaicharoen, and G. Raithel, Applied Physics Letters **104**, 244102 (2014), https://doi.org/10.1063/1.4883635.

[20] S. Kumar, H. Fan, H. Kubler, J. Sheng, and J. P. Shaffer, Scientific Reports **7**, 42981 (2017).

[21] J. A. Gordon, M. T. Simons, A. H. Haddab, and C. L. Holloway, AIP Advances **9**, 045030 (2019), https://doi.org/10.1063/1.5095633.

[22] M. Jing, Y. Hu, J. Ma, H. Zhang, L. Zhang, L. Xiao, and S. Jia, Nature Physics **16**, 911 (2020).

[23] M. T. Simons, J. A. Gordon, C. L. Holloway, D. A. Anderson, S. A. Miller, and G. Raithel, Applied Physics Letters **108**, 174101 (2016), http://dx.doi.org/10.1063/1.4947231.

[24] C. N. Cohen-Tannoudji, "The autler-townes effect revisited," in *Amazing Light: A Volume Dedicated To Charles Hard Townes On His 80th Birthday*, edited by R. Y. Chiao (Springer New York, New York, NY, 1996) pp. 109–123.

[25] D. A. Steck, "Cesium d line data," http://steck.us/alkalidata (1998), revision 2.1.6, 20 September 2013.

[26] M. Simons, M. D. Kautz, J. A. Gordon, and C. L. Holloway, in *Proc. of EMC Europe* (Amsterdam, the Netherlands, 2018).

[27] C. L. Holloway, M. T. Simons, J. A. Gordon, A. Dienstfrey, D. A. Anderson, and G. Raithel, Journal of Applied Physics **121**, 233106 (2017), http://dx.doi.org/10.1063/1.4984201.

[28] P. R. Berman and V. S. Malinovsky, *Principles of Laser Spectroscopy and Quantum Optics* (Princeton University Press, Princeton, 2011).